

Many-Body Factorization and Position-Momentum Equivalence of Nuclear Short-Range Correlations

R. Cruz-Torres,^{1,*} D. Lonardoni,^{2,3,*} R. Weiss,⁴ M. Piarulli,⁵ N. Barnea,⁴ D. W. Higinbotham,⁶ E. Piasetzky,⁷ A. Schmidt,¹ L. B. Weinstein,⁸ R. B. Wiringa,⁹ and O. Hen^{1,†}

¹*Massachusetts Institute of Technology, Cambridge, Massachusetts 02139, USA*

²*Facility for Rare Isotope Beams, Michigan State University, East Lansing, Michigan 48824, USA*

³*Theoretical Division, Los Alamos National Laboratory, Los Alamos, New Mexico 87545, USA*

⁴*Racah Institute of Physics, The Hebrew University, Jerusalem 91904, Israel*

⁵*Physics Department, Washington University, St Louis, MO 63130, USA*

⁶*Thomas Jefferson National Accelerator Facility, Newport News, Virginia 23606, USA*

⁷*School of Physics and Astronomy, Tel Aviv University, Tel Aviv 69978, Israel*

⁸*Old Dominion University, Norfolk, Virginia 23529, USA*

⁹*Physics Division, Argonne National Laboratory, Lemont, Illinois 60439, USA*

While mean-field approximations, such as the nuclear shell model, provide a good description of many bulk nuclear properties, they fail to capture the important effects of nucleon-nucleon correlations. Specifically, effective nuclear models struggle to describe the short-distance and high-momentum components of the nuclear many-body wave function. Here we study these components using the effective pair-based Generalized Contact Formalism (GCF) and ab-initio Quantum Monte Carlo (QMC) calculations of nuclei from deuteron to ^{40}Ca . We observe a universal factorization of the many-body nuclear wave function at short-distance into a strongly-interacting pair and a weakly-interacting residual system. The residual system distribution is consistent with that of an un-correlated system, showing that short-distance correlation effects are predominantly embedded in two-body correlations. We further find that the GCF accurately reproduces the many-body QMC calculations for both short distance and high momentum, supporting the dominance of two-nucleon short-range correlated (SRC) pairs in these components of the many-body wave function. Spin- and isospin-dependent “nuclear contact terms” are extracted in both coordinate and momentum space for different realistic nuclear potentials. The contact coefficient ratio between two different nuclei shows very little dependence upon the nuclear interaction model. These findings thus allow extending the application of mean-field approximations to SRC pair formation by showing that the relative abundance of *short-range* pairs in the nucleus is a *long-range* (*i.e.*, mean-field) quantity that is insensitive to the short-distance nature of the nuclear force.

Short-range correlations emerge from pairs of nucleons having large relative momentum compared to their center-of-mass (c.m.) momentum and to the typical nu-

clear Fermi momentum $k_F \approx 250 \text{ MeV/c}$ [1]. At momenta just above k_F ($300 \leq k \leq 600 \text{ MeV/c}$), they are primarily due to proton-neutron (pn) pairs and are thought to dominate the nuclear wave function [1–5]. At larger momentum, the fraction of proton-proton (pp) pairs increases, possibly due to their sensitivity to the repulsive core of the nuclear interaction [6, 7]. SRCs have significant implications for the internal structure of nucleons bound in nuclei [1, 8, 9], neutrinoless double beta decay matrix elements [10–12], nuclear charge radii [13], and neutron star properties [14, 15]. Therefore, understanding their formation mechanisms and specific characteristics is required for obtaining a complete description of atomic nuclei.

As nucleons in SRC pairs have significant spatial overlap and are far off their mass-shell ($E^2 - p^2 < m^2$), their theoretical description poses a significant challenge. Ab-initio many-body calculations using different interaction models produce wave functions that differ significantly at short distances and high momenta [16, 17] (Extended Data Fig. 1). This is generally referred to as “scale and scheme dependence”, where “scheme” refers to the type of interaction (*e.g.*, phenomenological or derived from Chiral Effective Field Theory, χEFT), and “scale” refers to the regulation cut-off inherent to EFT models. This dependence raises important questions about the model dependence of the interpretation of SRC measurements and of their implications.

To address this, we employ the pair-based GCF [18, 19] to study the scale and scheme dependence of different SRC properties, as extracted from many-body ab-initio QMC calculations of nuclei from $A = 2$ to 40 [16, 17, 20–23] performed using different realistic nuclear interaction models.

The GCF exploits the scale separation between the strong interaction among the nucleons in an SRC pair and the pair’s weaker interaction with its surroundings [18, 19, 24]. Using this scale separation, the two-nucleon density in either coordinate or momentum space (*i.e.*, probability of finding two nucleons with relative and

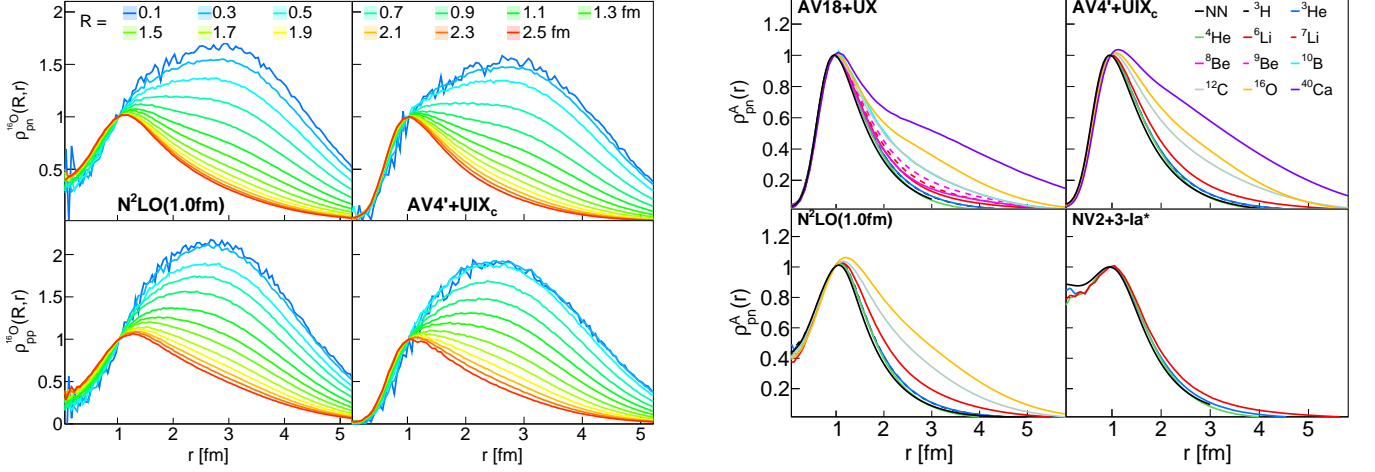


Figure 1: QMC two-nucleon coordinate-space densities calculated using different $NN+3N$ potentials. Left: ^{16}O relative-distance densities $\rho_{NN}^A(R, r)$ for pn (top) and pp (bottom) pairs for different regions in the nucleus (*i.e.*, different values of R) for two different interactions: $\text{AV4}' + \text{UIX}_c$ and $\text{N}^2\text{LO}(1.0\text{fm})$. Right: Relative-distance densities for pn pairs for several nuclei (colored lines) integrated over R and compared with the two-body universal function $|\varphi_{pn}^{s=1}|^2$ (black lines). For each interaction, all calculations are scaled to have the same value at ~ 1 fm, thus highlighting their same short-distance behavior for all nuclei. The difference between NN distributions in the same nucleus obtained using different interactions, as shown by the four panels, indicates the scale and scheme dependence of the many-body calculations. Equivalent pp distributions are presented in Extended Data Fig. 4.

c.m. momenta q and Q respectively, or with separation r and distance R from the nucleus c.m. [16]) can be expressed at small separation or high relative momentum as [19]:

$$\begin{aligned}\rho_{\alpha, NN}^A(R, r) &= C_{\alpha, NN}^A(R) \times |\varphi_{NN}^\alpha(r)|^2, \\ n_{\alpha, NN}^A(Q, q) &= \tilde{C}_{\alpha, NN}^A(Q) \times |\tilde{\varphi}_{NN}^\alpha(q)|^2,\end{aligned}\quad (1)$$

where A denotes the nucleus, NN the nucleon pair (pn , pp , nn), and α stands for the quantum state (spin 0 or 1). φ_{NN}^α are universal two-body wave functions, given by the zero-energy solution of the two-body Schrödinger equation, and $\tilde{\varphi}_{NN}^\alpha$ are their Fourier transforms. φ_{NN}^α are universal in the weak sense, *i.e.*, they are nucleus independent but not model independent. Nucleus-dependent “nuclear contact coefficients” are given by

$$\begin{aligned}C_{\alpha, NN}^A &\equiv \int d\mathbf{R} C_{\alpha, NN}^A(R), \\ \tilde{C}_{\alpha, NN}^A &\equiv \frac{1}{(2\pi)^3} \int d\mathbf{Q} \tilde{C}_{\alpha, NN}^A(Q),\end{aligned}\quad (2)$$

and define the number of NN -SRC pairs in nucleus A .

The GCF construction relates short-distance and high-momentum physics such that $C_{\alpha, NN}^A = \tilde{C}_{\alpha, NN}^A$. Previous studies [19] showed the validity of this equality using QMC calculations of $\rho_{\alpha, NN}^A(r) \equiv \int d\mathbf{R} \rho_{\alpha, NN}^A(R, r)$ and $n_{\alpha, NN}^A(q) \equiv \int d\mathbf{Q} n_{\alpha, NN}^A(Q, q)$ for $A = 2$ to 40 using the AV18 [25] + UX interaction. More recently, Refs. [23, 26] analyzed QMC calculations of $\rho_{NN}^A(r)/\rho_{NN}^d(r)$ ratios obtained using three additional interactions (without sepa-

rating different spin-isospin channels), showing first evidence for short distances scale-and-scheme independence.

Here we study the GCF applicability for modeling nuclear systems using new QMC calculations of $\rho_{\alpha, NN}^A(r, R)$ and $n_{\alpha, NN}^A(q, Q)$, projected into spin-isospin channels, for different nuclei and NN potentials ($\text{AV18} + \text{UX}$, $\text{AV4}' + \text{UIX}_c$, $\text{N}^2\text{LO}(1.0\text{fm})$, $\text{N}^2\text{LO}(1.2\text{fm})$, and $\text{NV2} + 3\text{-Ia}^*$). See Methods for details.

Fig. 1 (left) shows the relative-distance densities of np - and pp -pairs in Oxygen ^{16}O ($\rho_{NN}^A(R, r)$) for different values of R and for two different interactions: $\text{AV4}' + \text{UIX}_c$ and $\text{N}^2\text{LO}(1.0\text{fm})$. All densities were scaled to the same value at $r = 1$ fm. This highlights the similarities of the different distributions at $r \leq 1$ for all values of R , showcasing the existence of short-distance factorization.

Calculations of $\rho_{NN}^A(R, r)$ are computational demanding and are not available for all nuclei and interactions. We thus explore the nucleus and interaction independence of the short-distance factorization using $\rho_{NN}^A(r) = \int d\mathbf{R} \rho_{NN}^A(R, r)$ calculations. Fig. 1 (right) shows the pn -pair densities $\rho_{pn}^A(r)$ for four interactions and different nuclei. While the short-distance behavior of $\rho_{pn}^A(r)$ is different for each interaction, it is the same for all nuclei, and can thus be described by the GCF’s two-body universal functions. This validates the factorization of Eq. (1) in position space.

The equivalent study of two-nucleon momentum distributions $n_{NN}^A(q)$ is more delicate. $n_{NN}^A(Q, q)$ include combinatorial contributions from all possible pairs of nucleons, not just nucleon pairs in SRC states. Two nu-

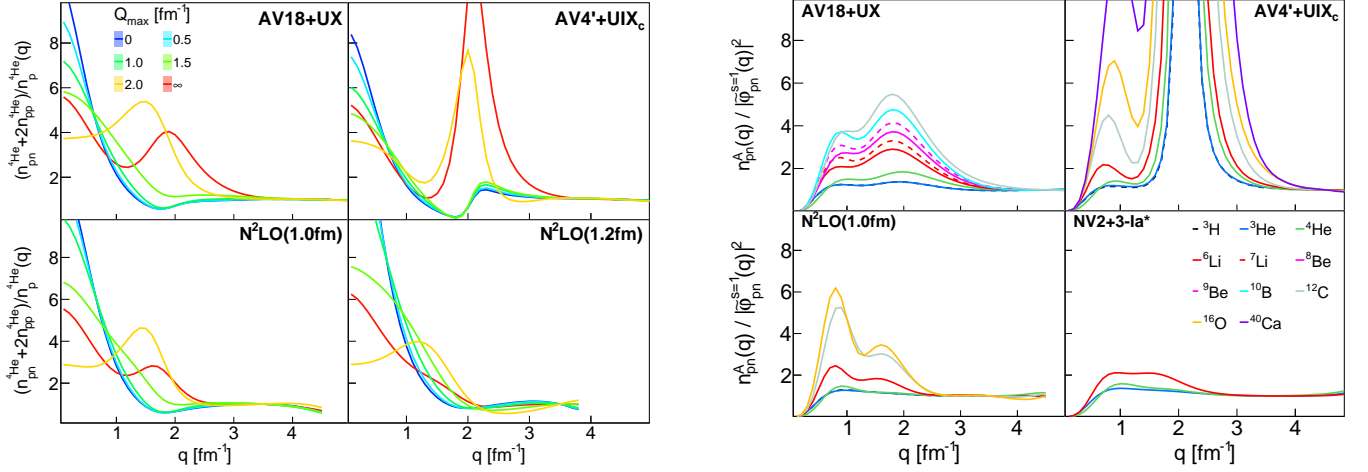


Figure 2: QMC two-nucleon momentum-space distributions calculated using different $NN+3N$ potentials. All the curves are normalized to unity at high momentum (4.5 fm^{-1} and 3.5 fm^{-1} for phenomenological and chiral interactions respectively). Left: ^4He relative-momentum distributions $n_{NN}^{4\text{He}}(Q, q)$ integrated over center-of-mass momentum Q between 0 and Q_{max} and divided by the one-body momentum distribution. Scaling onset is observed close to $q \approx k_F$ for Q_{max} between zero and k_F and is pushed to higher q values with increasing Q_{max} . Right: two-nucleon relative-momentum distribution ratios, $n_{pn}^A(q)/|\tilde{\varphi}_{pn}^{s=1}(q)|^2$, integrated over Q . Scaling is clearly observed at high-momenta, starting at $3.5 - 4 \text{ fm}^{-1}$ for the phenomenological potentials, and at $2 - 2.5 \text{ fm}^{-1}$ for the chiral interactions. The $N^2\text{LO}$ 1.0 fm and 1.2 fm distributions are only shown up to 4.4 and 3.8 fm^{-1} respectively, above which statistics is poor and regulator/cutoff artifacts dominate. Equivalent pp distributions are presented in Extended Data Fig. 4.

cleons each belonging to a different SRC pair have high individual momenta that can add to give both high relative and high c.m. momenta. In coordinate-space calculations these non-SRC pairs are suppressed by requiring small pair separation. In momentum space, excluding such pairs requires either low c.m. momenta or much higher relative momenta [19].

This can be seen by examining the q dependence of the ratio of the integrated two-body density to the one-body density in ^4He , $[\int_0^{Q_{max}} (n_{np}^{4\text{He}}(Q, q) + 2n_{pp}^{4\text{He}}(Q, q))dQ]/n_p^{4\text{He}}(q)$, for different values of Q_{max} , see Fig. 2 (left). Here $n_p^{4\text{He}}(q)$ is the probability density of finding a proton in the nucleus with momentum q . The ratio should scale (be constant with q) when both the one- and two-body densities are dominated by the same correlated SRC pairs. As can be seen, for Q_{max} values up to k_F (the characteristic c.m. momentum scale of SRC pairs [3, 24]) the ratio indeed starts scaling at $q \sim k_F$. For larger Q_{max} values, scaling starts at higher q values, due to the inclusion of uncorrelated pairs.

Fig. 2 (right) shows the $n_{pn}^A(q)/|\tilde{\varphi}_{pn}^{s=1}(q)|^2$ ratio for a variety of nuclei and interactions. As expected from Eq. (1), these ratios scale (*i.e.*, are constant) at high momenta. For pn pairs the scaling is clear. For pp pairs (Extended data Fig. 4) it is less pronounced, but it is still visible starting at slightly higher momenta than the equivalent pn scaling.

Having established the GCF factorization of Eq. (1), we turn to examine the nuclear contact terms $C_{\alpha, NN}^A$.

These encapsulate the many-body dynamics driving the formation of SRC pairs. They should be scale separated from the correlated two-body part and thus be less sensitive to the short-distance NN interaction.

Fig. 3 shows $C_{NN}^{16\text{O}}(R)$ for np - and pp -SRC pairs in oxygen, obtained using Eq. (1). The QMC contact distributions are in good agreement with calculations of uncorrelated pairs obtained from single-nucleon density distributions (see Methods for details). This agreement is insensitive to the pair separation integration limit from 0 to 1 fm. This shows that the density distribution of SRC pairs (*i.e.* shape of $C_{NN}^{16\text{O}}(R)$) only depends on the nuclear mean field, with minimal sensitivity to the short-distance NN interaction.

To further corroborate this finding and its relevance for other nuclei, we examine the ratio of two-nucleon distributions in nucleus A relative to a reference nucleus A_0 , *i.e.*, $\rho_{\alpha, NN}^A(r)/\rho_{\alpha, NN}^{A_0}(r)$ and $n_{\alpha, NN}^A(q)/n_{\alpha, NN}^{A_0}(q)$. According to Eq. (1), for small- r (large- q) these ratios should be independent of r (q) and equal to $C_{\alpha, NN}^A/C_{\alpha, NN}^{A_0}$ ($\tilde{C}_{\alpha, NN}^A/\tilde{C}_{\alpha, NN}^{A_0}$). They thus allow studying the A -dependence of the contacts, independent from the universal functions.

Fig. 4 shows $C_{s=1, pn}^A/C_{s=1, pn}^d$ and $C_{\alpha, NN}^A/C_{\alpha, NN}^{4\text{He}}$ for all available nuclei and interactions. The contact ratios for a given nucleus are consistent within uncertainties, *i.e.*, are largely scale- and scheme-independent. They are also the same for both short-distance and high-momentum pairs. The fact that models with very differ-

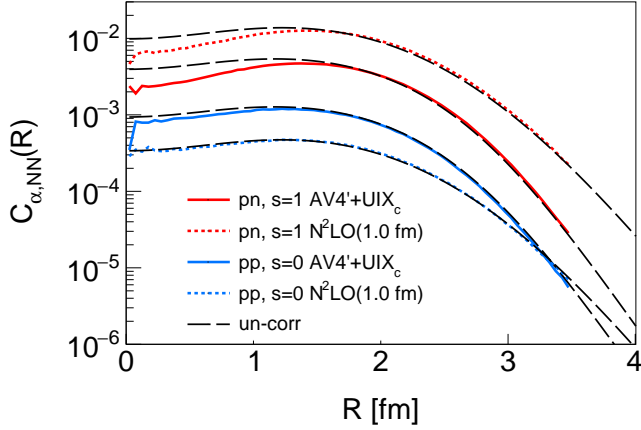


Figure 3: Absolute contact distributions $C_{\alpha, NN}^{16O}(R)$ obtained from QMC two-nucleon coordinate-space densities integrated over r from zero to 1 fm for pn (red) and pp (blue) pairs. The black curves correspond to extraction using un-correlated densities obtained using a convolution of the single-nucleon density distribution with itself. The un-correlated distributions are scaled by 0.87 (pp) and 0.65 (pn) to match the magnitude of the QMC distributions. See text for details.

ent short-range physics, including the tensor-less AV4', all lead to the same contact-term ratios supports our conclusion that these ratios are determined by mean-field physics (*i.e.*, by the average field of the other $A - 2$ nucleons) and are insensitive to the details of the NN interaction at short-distance.

This insensitivity can simplify calculations of heavier nuclei, that are very difficult with “hard” interactions such as AV18. The contact term $C_{\alpha, NN}^{A_0}$ can be calculated for d or ${}^4\text{He}$ using the “hard” interaction. It can then be extrapolated to heavier nuclei by multiplying by the appropriate contact-term ratio $C_{\alpha, NN}^A / C_{\alpha, NN}^{A_0}$ (where $A_0 = d$ or ${}^4\text{He}$) calculated using “soft” interactions that are easier to compute.

Experimentally, measured inclusive (e, e') scattering cross-section ratios at large momentum-transfer ($Q^2 > 1.5 \text{ GeV}^2$) for nucleus A relative to the deuteron are used to determine an SRC scaling coefficient $a_2(A/d)$. This coefficient is traditionally interpreted as the relative abundance of SRC pairs in the measured nuclei [27]. In addition, it is claimed that comparisons of $a_2(A/d)$ measurements over a range of symmetric and asymmetric nuclei are sensitive to the nature of the nuclear interaction.

Theoretically, Refs. [23, 26] showed that the relative abundance of short-distance NN pairs in nucleus A relative to the deuteron (*i.e.*, $\rho^A(r)/\rho^d(r)$ for $r \rightarrow 0$, where $\rho^A(r)$ includes all NN pairs) is insensitive to the choice of nuclear interaction, and is consistent with the measured $a_2(A/d)$ for all nuclei considered. This raised doubts about the sensitivity of $a_2(A/d)$ to the nuclear interaction. However, the connection between the measured

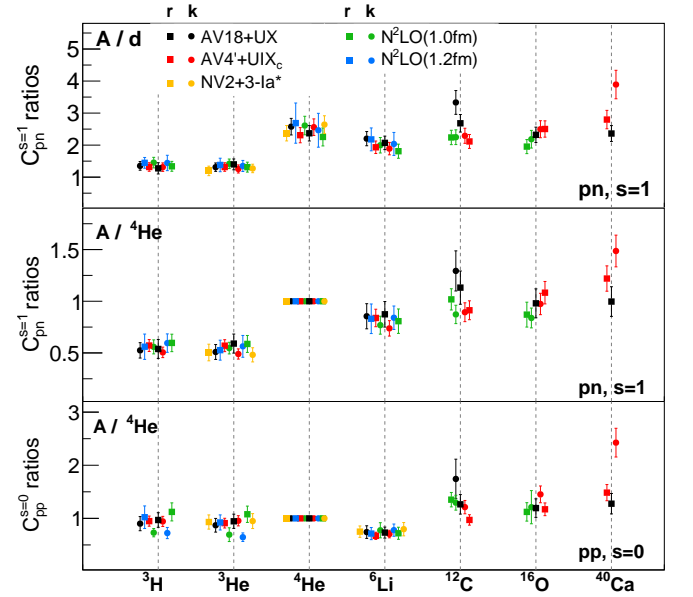


Figure 4: Ratios of spin-1 pn contact terms for different nuclei to deuteron (top) or ${}^4\text{He}$ (middle), and of spin-0 pp contact terms for different nuclei to ${}^4\text{He}$ (bottom). The contact terms ratios were extracted using different $NN+3N$ potentials in both coordinate (squares) and momentum (circles) space. The contact values for ${}^3\text{H}$ in the spin-0 pp panel corresponds to $C_{nn}^{s=0}({}^3\text{H})$, as there are no pp pairs in this nucleus. All the contacts $C_{NN}^\alpha(A)$ are divided by $A/2$ and multiplied by 100. Error bars show the combined statistical and extraction systematical uncertainties at the 1σ or 68% confidence level.

$a_2(A/d)$ and the calculated pair-distance distributions needs to be justified, as the universal function of Eq. 1 does not automatically cancel in the A/d ratio when all SRC channels are included [28]. Our observation that the calculated contact ratios are independent of the nuclear interaction in both coordinate and momentum space and for each pair quantum state separately bolsters and extends these observations.

Exclusive measurements of two-nucleon knockout $A(e, e' NN)$ [2–7] on the other hand are sensitive to the nuclear interaction model [6, 7] (see Extended Data Fig. 5). The GCF factorization, and the contact terms we extract, are key for relating measurements of nucleon knockout to different nuclear interaction models and ab-initio many-body calculations [6, 29, 30].

Ref. [31] recently claimed a difference between the scaling of SRC pairs with high relative momenta, dominated by pn pairs, and pairs with small separation, having a combinatorial enhancement of pp pairs. This distinction questions the relation between SRC pairs and the modification of the internal structure of nucleons bound in nuclei, extractions of the free neutron structure from nuclear deep inelastic scattering measurements, and the determination of spin-flavor symmetry breaking mecha-

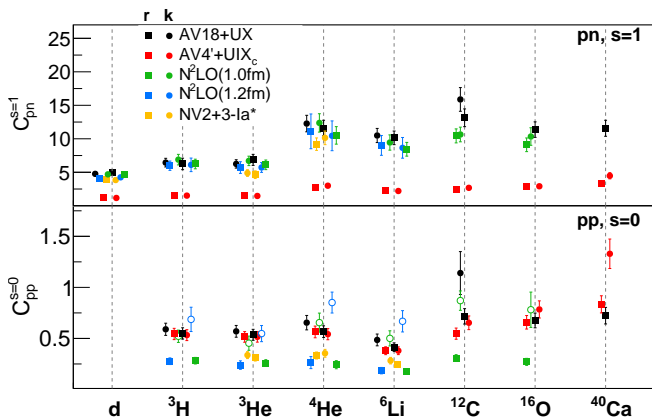


Figure 5: The absolute values of the spin-1 pn and spin-0 pp contact terms for different nuclei extracted from QMC calculations in both coordinate (squares) and momentum (circles) space using different $NN+3N$ potentials. The contact values for ${}^3\text{H}$ in the spin-0 pp panel corresponds to $C_{nn}^{s=0}({}^3\text{H})$, as there are no pp pairs in this nucleus. k -space N^2LO spin-0 pp contacts are marked with open symbols to highlight the difficulty in their extraction. See text for details. All the contacts $C_{NN}^a(A)$ are divided by $A/2$ and multiplied by 100. Error bars show the combined statistical and extraction systematical uncertainties at the 1σ or 68% confidence level.

nisms in QCD [9]. Our observation that both coordinate- and momentum-space contacts exhibit the same scaling show that the speculations of Ref. [31] are inconsistent with QMC wave functions [32].

Finally we examine the *individual* contacts. Fig. 5 and Extended Data Table II show the contacts extracted by fitting Eq. (1) to the individual two-nucleon QMC densities for different nuclei in either coordinate or momentum space. As can be seen, the extracted spin-1 pn contacts are scale- and scheme-independent (*i.e.*, the same) for all interactions examined here, except for the $\text{AV4}' + \text{UIX}_c$, as expected given its lack of a tensor force.

For spin-0 pp contacts our results are more complex. The contacts extracted for phenomenological potentials agree with each other but are higher than those extracted for chiral potentials. This is understood to result from the cutoffs employed in chiral interactions, that have a larger impact on the spin-0 pp channel due to the lack of a tensor force that otherwise would fill the minimum in the momentum distribution around 2 fm^{-1} (Extended Data Fig. 2).

Furthermore, the k -space N^2LO contacts disagree with their equivalent in r -space. As the $\text{NV2} + 3\text{-Ia}^*$ contacts do not show such a discrepancy, this issue is specific to the N^2LO potentials and is not an inherent feature of chiral potentials.

Examining the pp two-body universal functions we see that they are very similar for $\text{NV2} + 3\text{-Ia}^*$ and $\text{N}^2\text{LO}(1.0)$ (Extended Data Fig. 2). In contrast, the ${}^4\text{He}$ pp mo-

mentum distributions differ at high-momenta for the two potentials. This is most likely due to the combined effect of their different regulators, lower order in the chiral expansion, and lack of intermediate deltas in the N^2LO potential that enhances three-body effects that are absent in the GCF formulation of Eq. (1).

These regulator and three-body effects make it difficult to identifying a clear high-momentum scaling plateau in the spin-0 pp channel for N^2LO potentials. See Methods for details.

Indeed, when three-body forces and correlations are excluded from the calculation the k - and r -space N^2LO contacts are the same. Furthermore, the fact that the contact ratios of nucleus A to ${}^4\text{He}$ are the same in r - and k -space for all channels and interactions (including for N^2LO pp pairs) implies that the effect leading to the N^2LO pp r - k discrepancy cancels in the ratio, and therefore does not extend beyond the three-body level. We thus can conclude that (A) *the many-body ($A \geq 3$) nuclear dynamics of the contact coefficients is the same for both coordinate and momentum space and is independent of the details of the NN interaction model.* and (B) any corrections that are missing in Eq. (1), and cause the N^2LO discrepancy, do not involve terms that go beyond the three-body level, which is why they cancel in the ratios of heavy nuclei to light ones.

To conclude, the analysis presented here validates the scale-separated description of SRCs in atomic nuclei, as evident from the accurate reproduction of the many-body QMC calculations at short-distances and high-momenta provided by the GCF. We identify strong separation between the hard and soft dynamics of SRCs, where SRC abundances, and therefore their formation mechanisms, are observed to be governed by soft (mean-field like) nuclear dynamics, while their relative momentum distribution is a scale- and scheme-dependent property of the nuclear interaction. These findings have direct implications for experimental studies of SRCs [6, 30] and the interpretation of future measurements of SRC abundances and distributions in nuclei.

* Equal Contribution

† Contact author: hen@mit.edu

- [1] O. Hen, G. A. Miller, E. Piasetzky, and L. B. Weinstein, *Rev. Mod. Phys.* **89**, 045002 (2017).
- [2] R. Subedi *et al.*, *Science* **320**, 1476 (2008).
- [3] I. Korover *et al.*, *Phys. Rev. Lett.* **113**, 022501 (2014).
- [4] O. Hen *et al.* (CLAS Collaboration), *Science* **346**, 614 (2014).
- [5] M. Duer *et al.* (CLAS Collaboration), *Nature* **560**, 617 (2018).
- [6] A. Schmidt *et al.* (CLAS), *Nature* **578**, 540–544 (2020).
- [7] I. Korover *et al.* (CLAS), [arXiv:2004.07304 \[nucl-ex\]](https://arxiv.org/abs/2004.07304).
- [8] B. Schmookler *et al.* (CLAS), *Nature* **566**, 354 (2019).
- [9] E. P. Segarra, A. Schmidt, T. Kutz, D. W. Higinbotham,

- E. Piasetzky, M. Strikman, L. B. Weinstein, and O. Hen, *Phys. Rev. Lett.* **124**, 092002 (2020).
- [10] M. Kortelainen and J. Suhonen, *Phys. Rev. C* **76**, 024315 (2007).
- [11] F. Simkovic, A. Faessler, H. Muther, V. Rodin, and M. Stauf, *Phys. Rev. C* **79**, 055501 (2009).
- [12] V. Cirigliano, W. Dekens, J. De Vries, M. L. Graesser, E. Mereghetti, S. Pastore, and U. Van Kolck, *Phys. Rev. Lett.* **120**, 202001 (2018).
- [13] G. A. Miller, A. Beck, S. May-Tal Beck, L. B. Weinstein, E. Piasetzky, and O. Hen, *Phys. Lett. B* **793**, 360 (2019).
- [14] B.-A. Li, B.-J. Cai, L.-W. Chen, and J. Xu, *Prog. Part. Nucl. Phys.* **99**, 29 (2018).
- [15] L. Frankfurt, M. Sargsian, and M. Strikman, *Int. J. Mod. Phys. A* **23**, 2991 (2008).
- [16] R. B. Wiringa, R. Schiavilla, S. C. Pieper, and J. Carlson, *Phys. Rev. C* **89**, 024305 (2014).
- [17] D. Lonardoni, S. Gandolfi, X. B. Wang, and J. Carlson, *Phys. Rev. C* **98**, 014322 (2018).
- [18] R. Weiss, B. Bazak, and N. Barnea, *Phys. Rev. C* **92**, 054311 (2015).
- [19] R. Weiss, R. Cruz-Torres, N. Barnea, E. Piasetzky, and O. Hen, *Phys. Lett. B* **780**, 211 (2018).
- [20] D. Lonardoni, A. Lovato, S. C. Pieper, and R. B. Wiringa, *Phys. Rev. C* **96**, 024326 (2017).
- [21] D. Lonardoni, J. Carlson, S. Gandolfi, J. E. Lynn, K. E. Schmidt, A. Schwenk, and X. B. Wang, *Phys. Rev. Lett.* **120**, 122502 (2018).
- [22] D. Lonardoni, S. Gandolfi, J. E. Lynn, C. Petrie, J. Carlson, K. E. Schmidt, and A. Schwenk, *Phys. Rev. C* **97**, 044318 (2018).
- [23] J. Lynn, D. Lonardoni, J. Carlson, J. Chen, W. Detmold, S. Gandolfi, and A. Schwenk, *J. Phys. G* **47**, 045109 (2020).
- [24] E. O. Cohen *et al.* (CLAS Collaboration), *Phys. Rev. Lett.* **121**, 092501 (2018).
- [25] R. B. Wiringa, V. G. J. Stoks, and R. Schiavilla, *Phys. Rev. C* **51**, 38 (1995).
- [26] J.-W. Chen, W. Detmold, J. E. Lynn, and A. Schwenk, *Phys. Rev. Lett.* **119**, 262502 (2017).
- [27] K. S. Egiyan *et al.* (CLAS Collaboration), *Phys. Rev. C* **68**, 014313 (2003).
- [28] R. Weiss, A. Denniston, J. Pybus, O. Hen, E. Piasetzky, A. Schmidt, L. Weinstein, and N. Barnea, *arXiv:2005.01621 [nucl-th]*.
- [29] R. Weiss, I. Korover, E. Piasetzky, O. Hen, and N. Barnea, *Phys. Lett. B* **791**, 242 (2019).
- [30] J. Pybus, I. Korover, R. Weiss, A. Schmidt, N. Barnea, D. Higinbotham, E. Piasetzky, M. Strikman, L. Weinstein, and O. Hen, *Phys. Lett. B* **805**, 135429 (2020).
- [31] J. Arrington and N. Fomin, *Phys. Rev. Lett.* **123**, 042501 (2019).
- [32] O. Hen, F. Hauenstein, D. W. Higinbotham, G. A. Miller, E. Piasetzky, A. Schmidt, E. P. Segarra, M. Strikman, and L. B. Weinstein, *arXiv:1905.02172 [nucl-ex]*.
- [33] R. B. Wiringa and S. C. Pieper, *Phys. Rev. Lett.* **89**, 182501 (2002).
- [34] A. Gezerlis, I. Tews, E. Epelbaum, M. Freunek, S. Gandolfi, K. Hebeler, A. Nogga, and A. Schwenk, *Phys. Rev. C* **90**, 054323 (2014).
- [35] J. E. Lynn, I. Tews, J. Carlson, S. Gandolfi, A. Gezerlis, K. E. Schmidt, and A. Schwenk, *Phys. Rev. Lett.* **116**, 062501 (2016).
- [36] M. Piarulli, L. Girlanda, R. Schiavilla, A. Kievsky, A. Lovato, L. E. Marcucci, S. C. Pieper, M. Viviani, and R. B. Wiringa, *Phys. Rev. C* **94**, 054007 (2016).
- [37] M. Piarulli *et al.*, *Phys. Rev. Lett.* **120**, 052503 (2018).
- [38] A. Baroni, R. Schiavilla, L. E. Marcucci, L. Girlanda, A. Kievsky, A. Lovato, S. Pastore, M. Piarulli, S. C. Pieper, M. Viviani, and R. B. Wiringa, *Phys. Rev. C* **98**, 044003 (2018).
- [39] R. Cruz-Torres, A. Schmidt, G. A. Miller, L. B. Weinstein, N. Barnea, R. Weiss, E. Piasetzky, and O. Hen, *Phys. Lett. B* **785**, 304 (2018).
- [40] B. S. Pudliner, V. R. Pandharipande, J. Carlson, S. C. Pieper, and R. B. Wiringa, *Phys. Rev. C* **56**, 1720 (1997).

Acknowledgments We thank J. E. Lynn for providing some of the deuteron momentum distributions. We are also thankful to J. Carlson, C. Ciofi degli Atti, W. Cosyn, S. Gandolfi, A. Lovato, G.A. Miller, J. Ryckebusch, M. Sargsian, and M. Strikman for many insightful discussions. This work was supported by the U.S. Department of Energy, Office of Science, Office of Nuclear Physics under Award Numbers DE-FG02-94ER40818, DE-FG02-96ER-40960, DE-AC02-06CH11357, DE-SC0013617 and DE-AC05-06OR23177, the Pazy foundation, and the Israeli Science Foundation (Israel) under Grants Nos. 136/12 and 1334/16, the NUCLEI SciDAC program, the INCITE program, and the Clore Foundation. Computational resources have been provided by the Los Alamos Open Supercomputing via the Institutional Computing (IC) program, by the Argonne Leadership Computing Facility at Argonne National Laboratory, which is supported by the U.S. Department of Energy, Office of Science, under Contract No. DE-AC02-06CH11357, and by the National Energy Research Scientific Computing Center (NERSC), which is supported by the U.S. Department of Energy, Office of Science, under Contract No. DE-AC02-05CH11231.

Author Contributions D.L., M.P. and R.B.W. performed the many-body QMC calculations. N.B. and R.W. calculated the two-body universal functions. R.C.T and R.W. analyzed the QMC calculated densities and extracted the nuclear contacts. N.B., D.W.H., E.P., A.S., L.B.W., and O.H. initiated and guided the work. All authors contributed to writing the paper and reviewing the results.

Competing interests The authors declare no competing interests.

Data Availability The calculated densities that support the findings of this study are available from the corresponding author upon request.

Author Information Reprints and permissions information is available at www.nature.com/reprints. Readers are welcome to comment on the online version of the paper. Publisher's note: Springer Nature remains

neutral with regard to jurisdictional claims in published maps and institutional affiliations. Correspondence and requests for materials should be addressed to O.H. (hen@mit.edu).

Methods

Universal function normalization. While the normalizations of two-nucleon densities are well defined by the total number of nucleons in the nucleus, the individual normalizations of $C_{\alpha,NN}^A$ and $|\varphi_{NN}^\alpha|^2$ are not. We therefore choose to normalize $|\tilde{\varphi}_{NN}^\alpha(q)|^2$ such that its integral above $q_s = 1.3 \text{ fm}^{-1} (\approx k_F)$ equals unity [19], $\int_{q_s}^{\infty} \frac{4\pi}{(2\pi)^3} q^2 dq |\tilde{\varphi}_{NN}^\alpha(q)|^2 = 1$. This defines the normalization of $\varphi_{NN}^\alpha(r)$ via a Fourier transform and that of $C_{\alpha,NN}^A$ and $\tilde{C}_{\alpha,NN}^A$ via Eq. (1).

Nucleon-Nucleon interaction models. The phenomenological AV18 [25] and AV4' [33] potentials are “hard interactions”, with a significant probability for nucleons to have high momentum ($k > 3 \text{ fm}^{-1} \approx 600 \text{ MeV}/c$). Their derivation is similar, with AV4' being a reprojection of AV18 into four spin-isospin channels, not including the tensor interaction. Both potentials are supported by $3N$ forces that provide a good description of all nuclei considered in this work [20, 23].

The $N^2\text{LO}$ [22, 34, 35] and $\text{NV}2+3\text{-Ia}^*$ [36–38] interactions are fundamentally different, as they are based on a chiral perturbation expansion. The short-distance regulators used in these potentials make them softer, *i.e.*, their single-nucleon momentum distributions have less high-momentum strength as compared to AV18 and AV4' (see Extended Data Figs. 1 and 2). The $N^2\text{LO}$ interactions include operators up to third order in the chiral expansion. The $\text{NV}2+3\text{-Ia}^*$ interaction considers nucleons plus explicit intermediate deltas, and includes all terms up to third order plus leading order $N^3\text{LO}$ terms.

All NN potentials used in this work have accompanying $3N$ potentials (three-body forces or 3BF) optimized to properly describe properties of light nuclei, such as binding energies, n - α scattering, and β -decay rates.

QMC calculations. The QMC calculations used in this work include both Variational Monte Carlo (VMC) and Diffusion Monte Carlo (DMC) techniques. For each potential, a fully correlated many-body wave function is constructed and optimized in order to minimize the variational energy expectation value. Such a trial wave function is then propagated in imaginary time via DMC techniques, in order to project it onto the true ground state of the system and, therefore, to gain access to ground-state properties. Many physical quantities, such as two-nucleon distributions, can be extracted from both VMC and DMC calculations [22]. However, momentum-space calculations are currently available from VMC calculations only [16, 17], therefore for consistency we only present VMC results. At short distance, VMC coordinate-space distributions are almost identical to the DMC results. We use the differences as a measure of the QMC uncertainty (Extended Data Fig. 3).

Un-correlated two-nucleon density calculations.

Un-correlated two-nucleon densities are given by a convolution of the single-nucleon density distribution, $\rho_N^{16\text{O}}(R)$, with itself, $C_{NN,un-corr.}^{16\text{O}}(R) \equiv \int_0^{1 \text{ fm}} d\Omega_R d\mathbf{r} \rho_N^{16\text{O}}(\mathbf{R} + \mathbf{r}/2) \rho_N^{16\text{O}}(\mathbf{R} - \mathbf{r}/2)$, accounting for the Pauli exclusion principle for pp pairs, following Ref. [39]. The two-body density is normalized to the number of nucleon pairs in the nucleus.

Nuclear contact extraction. The nuclear contact terms were extracted independently for both coordinate and momentum space by fitting the universal two-body wave functions in coordinate and momentum-space to the corresponding two-body coordinate density or momentum distribution. Since all the spin and isospin projections are not available for the two-body momentum and coordinate densities, for $C_{pp}^{s=0}$ we fit the total pp distribution assuming that the dominant contribution comes from spin=0 (S -wave) pairs. Furthermore, for $C_{pn}^{s=1} (C_{pn}^{s=0})$ we fit to the $T = 0$ ($T = 1$) pn distributions assuming that the dominant contribution comes from spin=1 (spin=0) pairs with the relevant angular momentum.

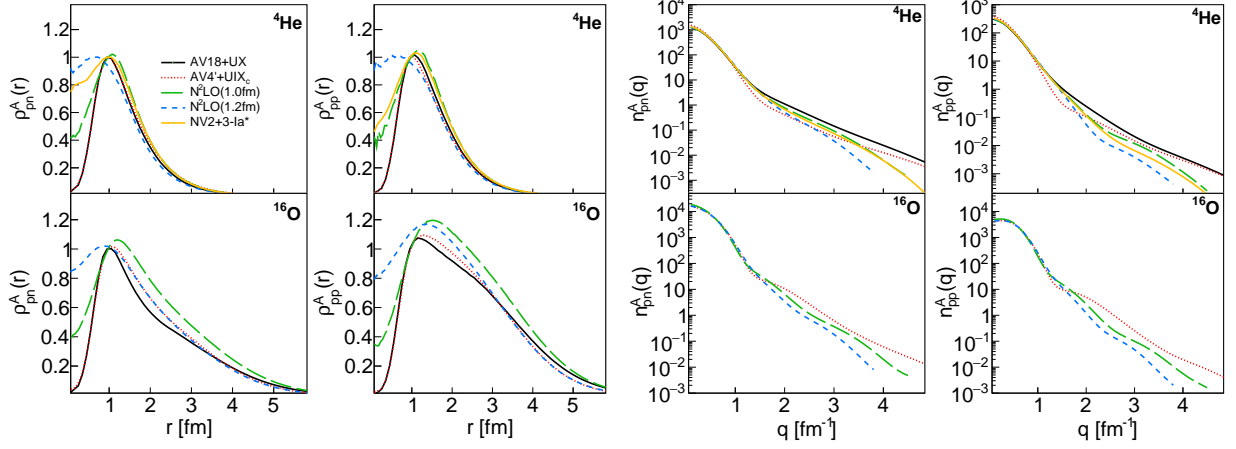
The ratios were extracted independently for both coordinate and momentum space by fitting the two-nucleon density ratios at short distance or high momentum, respectively [19].

The uncertainties shown include contributions from sensitivity to the fit range, the effect of different two-body correlations [22], the structure of the three-body contact interaction (for $N^2\text{LO}$ potentials), and the difference between different QMC techniques, conservatively fixed at 10% (1σ). See Supplementary Materials for details.

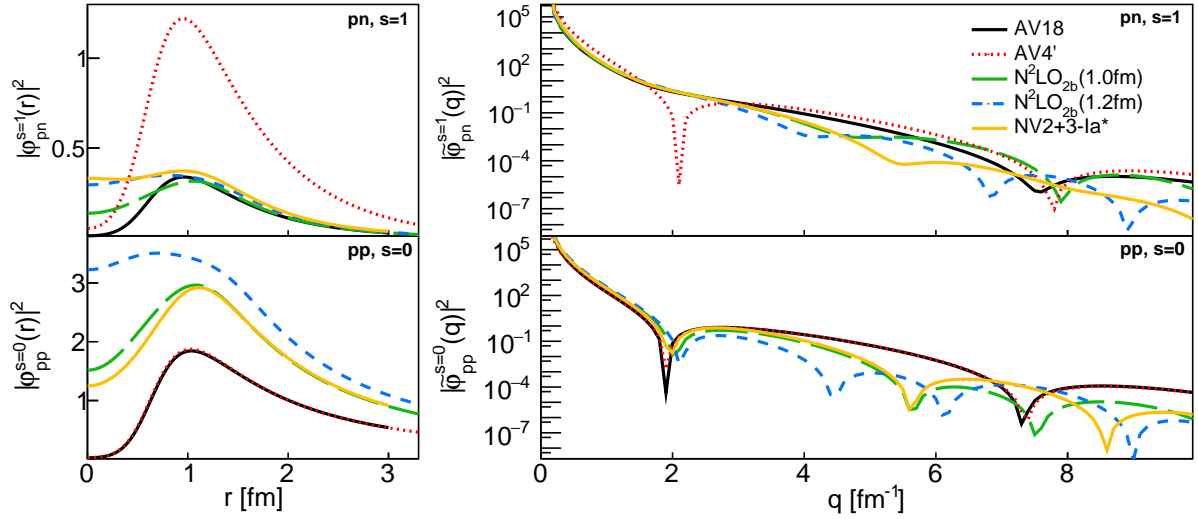
$N^2\text{LO}$ high-momentum scaling. The nuclear contact extraction is done systematically in the region $2.5 \lesssim q \lesssim 4.5 \text{ fm}^{-1}$ for all NN channels and potentials, as described above. Extended Data Fig. 7 shows the two-nucleon relative-momentum distribution ratios, $n_{NN}(q)/|\tilde{\varphi}_{NN}(q)|^2$, in ^4He for spin-1 pn and spin-0 pp channels and different interactions. In order to resolve possible higher-momentum effects, additional statistics has been used to compute the two-body momentum distributions shown in the figure. Discontinuities in the ratios are due to nodes in the corresponding universal functions (see Extended Data Fig. 2). For the AV4'+UIX_c and NV2+3-Ia* interactions, plateaus are clearly identifiable in both the spin-1 pn and spin-0 pp channels, and they consistently extend to very high momentum. For $N^2\text{LO}$ interactions, in the spin-1 pn channel more complex structures appear, but the contact values extracted at lower momentum remain consistent within uncertainties. In the spin-0 pp channel, instead, a clear high-momentum scaling is difficult to identify, leading to

the apparent spin-0 pp r - k discrepancy for N²LO interactions. This artifact is most likely related to regulator and three-body artifacts, and induced by the occurrence of multiple nearby nodes in the corresponding universal functions. The coordinate-space regulator employed in the NV2+3-Ia* interaction has a Gaussian form [36], that transforms in a Gaussian regulator in momentum space. The N²LO interactions use a different local regulator [34], that does not keep the same functional form when transformed to momentum space and can induce wiggles at high momentum. When the universal function has a quick drop, like in such a wiggle or in a node, the contribution of two-body SRCs is suddenly decreased, and other contributions become non negligible, complicating the overall picture and its interpretation.

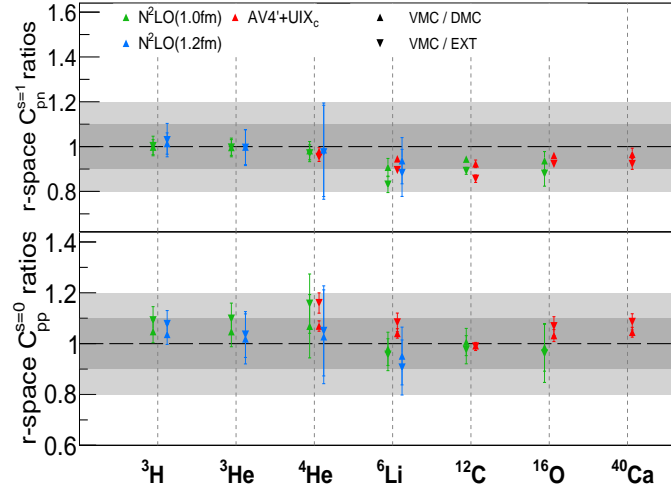
Extended Data



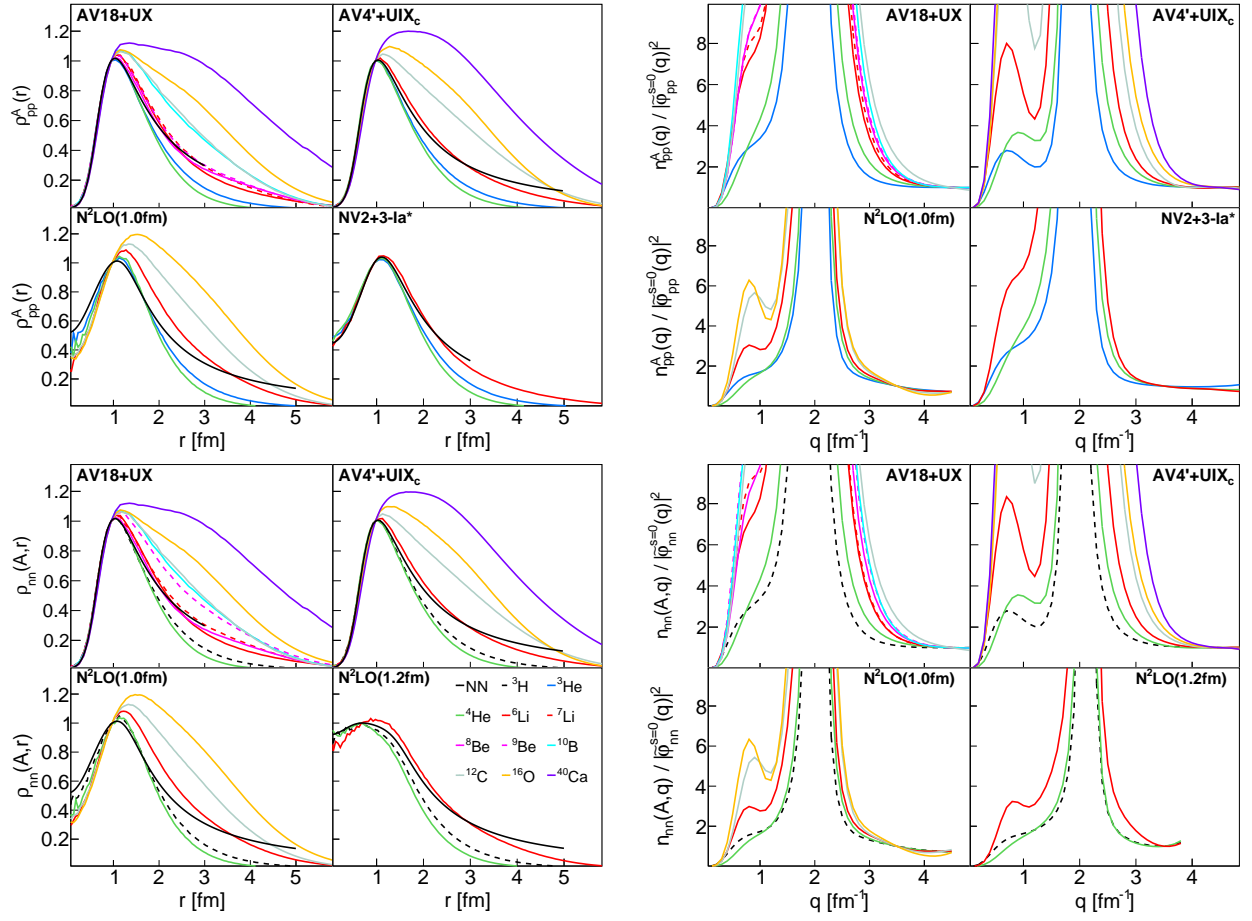
Extended Data Fig. 1: Scale and Scheme dependence of two-nucleon densities. Two-nucleon coordinate (left two columns) and momentum (right two columns) space distributions calculated using different $NN+3N$ potentials for different nuclei. The top and bottom rows show distributions for ^4He and ^{16}O respectively.



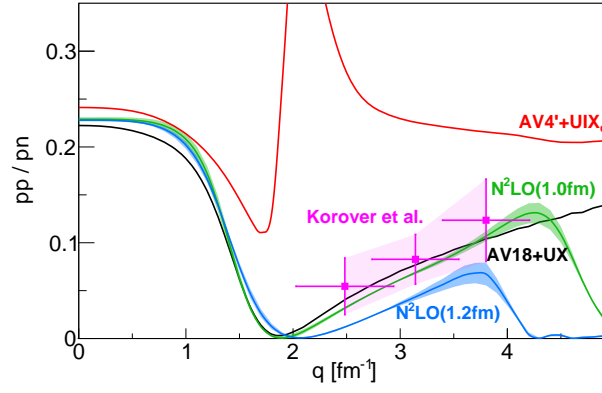
Extended Data Fig. 2: Universal two-body functions. NN interaction model dependence of the universal two-body functions $|\varphi_{NN}^\alpha|^2$ for spin-1 pn (top) and spin-0 pp (bottom) pairs calculated in both coordinate (left) and momentum (right).



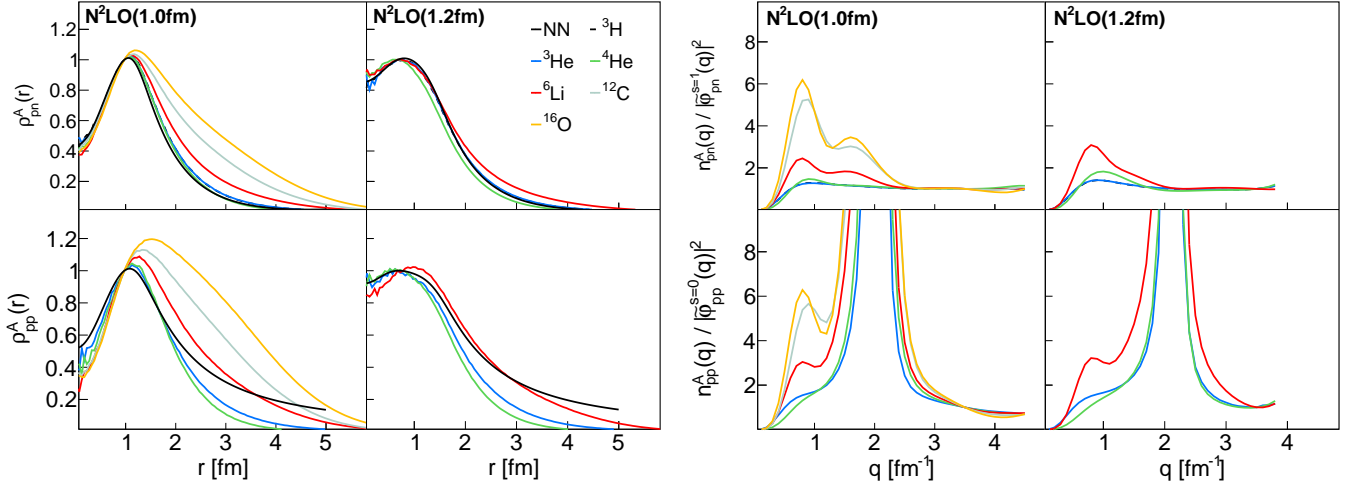
Extended Data Fig. 3: Calculation accuracy estimation. Ratios of contacts extracted from VMC densities to contacts extracted from DMC and extrapolated (EXT = $2 \times \text{DMC} - \text{VMC}$ [22]) distributions. Error bars show the combined statistical and extraction systematical uncertainties at the 1σ or 68% confidence level.



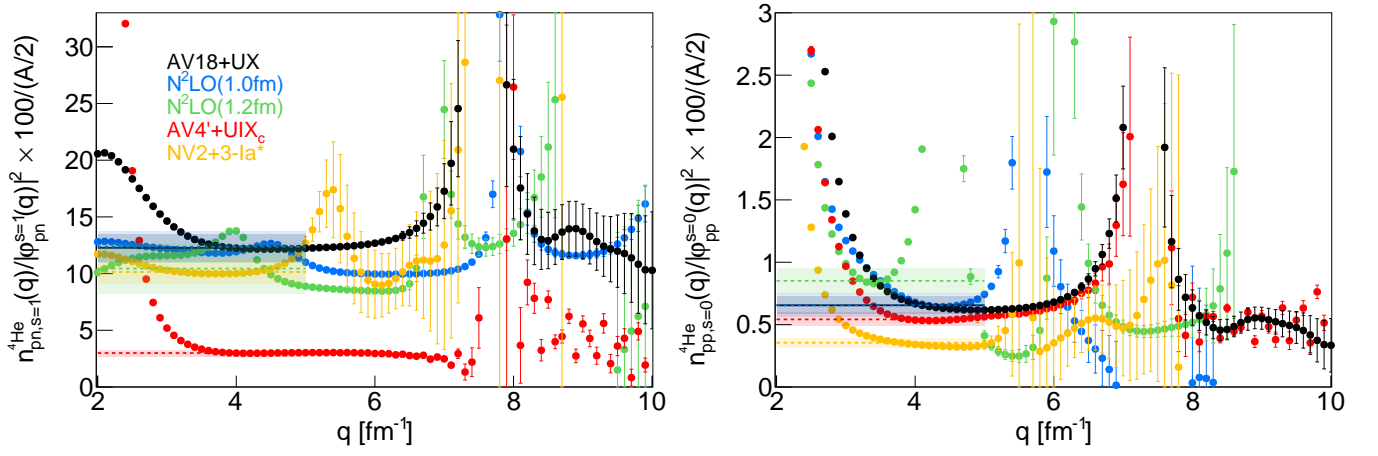
Extended Data Fig. 4: pp and nn two-nucleon distributions. Same as Fig. 2 but for pp (top) and nn (bottom) distributions.



Extended Data Fig. 5: pp -to- pn pairs ratio from experiment and theory. Ratio of pp -to- pn back-to-back pairs in ${}^4\text{He}$ as a function of pair relative momentum q , $n_{pp}(Q=0, q)/n_{pn}(Q=0, q)$, for different $NN+3N$ potentials, compared with the experimental extractions of Ref. [3] using $(e, e'pp)$ and $(e, e'pn)$ data. Data error bars show the combined statistical and systematical uncertainties at the 1σ or 68% confidence level.



Extended Data Fig. 6: Comparison between QMC calculations carried out with the $N^2\text{LO}$ potential with 1.0 fm and 1.2 fm short-distance cutoffs. Left: Relative-distance densities for pn (top) and pp (bottom) pairs for several nuclei (colored lines) integrated over R and compared with the two-body universal functions (black lines). For each interaction, all calculations are scaled to have the same value at ~ 1 fm and show the same short-distance behavior for all nuclei. Right: same as the left panel but for the two-nucleon momentum-space distribution ratios, $n_{pn}^A(q)/|\tilde{\varphi}_{pn}^{s=1}(q)|^2$ (top) and $n_{pp}^A(q)/|\tilde{\varphi}_{pp}^{s=0}(q)|^2$ (bottom), normalized to unity at $q = 3.5 \text{ fm}^{-1}$. Scaling is clearly observed at high momenta. The $N^2\text{LO}$ 1.0 fm and 1.2 fm distributions are only shown up to 4.4 and 3.8 fm^{-1} respectively, above which statistics is poor and regulator/cutoff artifacts dominate.



Extended Data Fig. 7: ${}^4\text{He}$ two-nucleon relative-momentum distribution ratios, $n_{NN}(q)/|\tilde{\varphi}_{NN}(q)|^2$. Left: spin-1 pn . Right: spin-0 pp . All curves are divided by $A/2 = 2$ and multiplied by 100. Results for five potentials are shown: AV18+UX, AV4'+UIX_c, NV2+3-Ia*, N²LO $R_0 = 1.0$ fm, and N²LO $R_0 = 1.2$ fm. Horizontal lines with error bands correspond to the extracted contacts (see Methods and Extended Data Table II). For N²LO potentials, results for one choice of three-body contact operators is shown here.

Extended Data Table I: Nuclei and Models included in this study. QMC-calculated two-nucleon distributions for different nuclei and $NN+3N$ potentials. Checkmarks indicate calculations used in the current study. All calculations are available for both coordinate and momentum space, except for ${}^{16}\text{O}$ and ${}^{40}\text{Ca}$ with AV18 (labeled with an * below), for which the UIX potential is used and results are only available in coordinate space [20]. Calculations with the N²LO (1.2 fm) potential for heavier systems are not considered in this work due to the large regulator artifacts found for $A \geq 12$ (see Ref. [22]).

Nucleus	AV18+UX [16, 25, 40]	AV4'+UIX _c [23, 33]	N ² LO(1.0fm) [22, 34, 35]	N ² LO(1.2fm) [22, 34, 35]	NV2+3-Ia* [36, 37]
d	✓	✓	✓	✓	✓
${}^3\text{H}$	✓	✓	✓	✓	—
${}^3\text{He}$	✓	✓	✓	✓	✓
${}^4\text{He}$	✓	✓	✓	✓	✓
${}^6\text{Li}$	✓	✓	✓	✓	✓
${}^{12}\text{C}$	✓	✓	✓	—	—
${}^{16}\text{O}$	✓*	✓	✓	—	—
${}^{40}\text{Ca}$	✓*	✓	—	—	—

* calculation only available for coordinate-space distributions.

Extended Data Table II: Nuclear contacts values. The extracted contact values have been divided by $A/2$ and multiplied by 100 to give the percent of nucleons above k_F . For symmetric nuclei, $C_{nn}^{s=0} = C_{pp}^{s=0}$. In the case of ${}^3\text{He}$, $C_{nn}^{s=0} = 0$, as there is only one neutron in this nucleus. In the case of ${}^3\text{H}$, $C_{pp}^{s=0} = 0$, as there is only one proton in this nucleus, and the values shown under $C_{pp}^{s=0}$ correspond to $C_{nn}^{s=0}$.

		$C_{pn}^{s=1}$		$C_{pp}^{s=0}$		$C_{pn}^{s=0}$	
		r	k	r	k	r	k
d	AV18	4.898 ± 0.080	4.764 ± 0.007				
	AV4'	1.186 ± 0.034	1.165 ± 0.037				
	N ² LO(1.0)	4.664 ± 0.009	4.691 ± 0.030				
	N ² LO(1.2)	4.141 ± 0.010	4.244 ± 0.032				
	NV2+3-Ia*	3.878 ± 0.390	3.840 ± 0.398				
${}^3\text{H}$	AV18	6.246 ± 0.856	6.441 ± 0.645	0.549 ± 0.055	0.590 ± 0.060	0.295 ± 0.119	0.311 ± 0.033
	AV4'	1.533 ± 0.154	1.515 ± 0.152	0.544 ± 0.055	0.532 ± 0.054	0.270 ± 0.027	0.281 ± 0.029
	N ² LO(1.0)	6.237 ± 0.718	6.885 ± 0.789	0.282 ± 0.032	0.521 ± 0.060	0.140 ± 0.015	0.255 ± 0.063
	N ² LO(1.2)	5.980 ± 0.695	6.111 ± 1.011	0.277 ± 0.033	0.687 ± 0.119	0.139 ± 0.017	0.337 ± 0.061
${}^3\text{He}$	AV18	6.851 ± 0.822	6.249 ± 0.625	0.536 ± 0.054	0.570 ± 0.058	0.161 ± 0.092	0.325 ± 0.034
	AV4'	1.527 ± 0.153	1.466 ± 0.147	0.515 ± 0.052	0.515 ± 0.052	0.265 ± 0.027	0.264 ± 0.028
	N ² LO(1.0)	6.113 ± 0.719	6.703 ± 0.702	0.259 ± 0.032	0.454 ± 0.069	0.135 ± 0.016	0.264 ± 0.047
	N ² LO(1.2)	5.705 ± 0.870	5.717 ± 0.730	0.239 ± 0.041	0.547 ± 0.079	0.127 ± 0.022	0.307 ± 0.057
	NV2+3-Ia*	4.637 ± 0.573	4.885 ± 0.491	0.310 ± 0.031	0.336 ± 0.034	0.234 ± 0.053	0.233 ± 0.024
${}^4\text{He}$	AV18	11.605 ± 1.161	12.274 ± 1.232	0.567 ± 0.057	0.655 ± 0.071	0.567 ± 0.057	0.687 ± 0.075
	AV4'	2.685 ± 0.272	2.995 ± 0.300	0.564 ± 0.057	0.542 ± 0.055	0.578 ± 0.059	0.564 ± 0.057
	N ² LO(1.0)	10.508 ± 1.308	12.372 ± 1.372	0.243 ± 0.040	0.655 ± 0.093	0.253 ± 0.043	0.703 ± 0.096
	N ² LO(1.2)	11.111 ± 2.595	10.446 ± 2.223	0.263 ± 0.059	0.851 ± 0.102	0.281 ± 0.062	0.934 ± 0.133
	NV2+3-Ia*	9.200 ± 0.928	10.143 ± 1.022	0.333 ± 0.034	0.355 ± 0.039	0.333 ± 0.034	0.504 ± 0.059
${}^6\text{Li}$	AV18	10.140 ± 1.015	10.492 ± 1.056	0.415 ± 0.042	0.485 ± 0.058	0.415 ± 0.042	0.529 ± 0.071
	AV4'	2.248 ± 0.225	2.205 ± 0.222	0.380 ± 0.038	0.380 ± 0.038	0.387 ± 0.039	0.369 ± 0.039
	N ² LO(1.0)	8.434 ± 1.026	9.444 ± 1.141	0.173 ± 0.020	0.501 ± 0.074	0.180 ± 0.021	0.540 ± 0.086
	N ² LO(1.2)	9.011 ± 1.478	8.650 ± 1.545	0.185 ± 0.031	0.668 ± 0.104	0.197 ± 0.034	0.749 ± 0.168
	NV2+3-Ia*			0.250 ± 0.025	0.282 ± 0.032		
${}^{12}\text{C}$	AV18	13.135 ± 1.324	15.876 ± 1.770	0.716 ± 0.075	1.140 ± 0.210	0.716 ± 0.075	1.244 ± 0.319
	AV4'	2.458 ± 0.249	2.676 ± 0.272	0.547 ± 0.055	0.653 ± 0.067	0.559 ± 0.056	0.558 ± 0.069
	N ² LO(1.0)	10.434 ± 1.044	10.643 ± 1.094	0.308 ± 0.033	0.870 ± 0.095	0.318 ± 0.034	0.988 ± 0.161
${}^{16}\text{O}$	AV18	11.372 ± 1.158		0.676 ± 0.072		0.676 ± 0.072	
	AV4'	2.910 ± 0.293	2.911 ± 0.307	0.658 ± 0.066	0.784 ± 0.084	0.675 ± 0.068	0.702 ± 0.086
	N ² LO(1.0)	9.103 ± 1.020	10.338 ± 1.310	0.270 ± 0.034	0.781 ± 0.173	0.275 ± 0.033	0.928 ± 0.365
${}^{40}\text{Ca}$	AV18	11.570 ± 1.196		0.723 ± 0.081		0.723 ± 0.081	
	AV4'	3.284 ± 0.339	4.476 ± 0.460	0.834 ± 0.084	1.329 ± 0.144	0.854 ± 0.086	1.357 ± 0.164